

Digital Mechanical Metamaterial: Encoding Mechanical Information with Graphical Stiffness Pattern for Adaptive Soft Machines

Jun Kyu Choe, Jiyeon Yi, Hanhyeok Jang, Heejae Won, Suwoo Lee, Hajun Lee, Yeonwoo Jang, Hyeonseong Song, and Jiyun Kim*

Inspired by the adaptive features exhibited by biological organisms like the octopus, soft machines that can tune their shape and mechanical properties have shown great potential in applications involving unstructured and continuously changing environments. However, current soft machines are far from achieving the same level of adaptability as their biological counterparts, hampered by limited real-time tunability and severely deficient reprogrammable space of properties and functionalities. As a steppingstone toward fully adaptive soft robots and smart interactive machines, an encodable multifunctional material that uses graphical stiffness patterns is introduced here to in situ program versatile mechanical capabilities without requiring additional infrastructure. Through independently switching the digital binary stiffness states (soft or rigid) of individual constituent units of a simple auxetic structure with elliptical voids, in situ and gradational tunability is demonstrated here in various mechanical qualities such as shape-shifting and -memory, stress–strain response, and Poisson's ratio under compressive load as well as application-oriented functionalities such as tunable and reusable energy absorption and pressure delivery. This digitally programmable material is expected to pave the way toward multienvironment soft robots and interactive machines.

have been appealing candidates for the creation of intelligent adaptive devices, soft robots, and machines.^[1–10] One promising approach toward programmable systems is to use mechanical metamaterials, a class of artificially designed material that gains global scale mechanical properties from the local scale structural patterns, which have shown great capabilities to enable various exotic physical properties such as programmable shape-shifting,^[11–15] negative and alternating Poisson's ratio,^[16,17] tunable stress–strain curve,^[18–20] and tunable impact energy absorption.^[21] However, these exhibited features are often specifically programmed during the design stage and cannot be reprogrammed postfabrication to accommodate a range of tasks. While some mechanical metamaterials are designed to reversibly go between different configurations using interchangeable bistable and multistable geometries,^[22–24] the achievable properties are highly constrained by the prescribed design and may use structures that are not scalable and cannot serve as a building block of a multifunctional mechanical metamaterial.

1. Introduction

Soft materials having elasticity similar to that of biological tissues are finding increasing utility in versatile systems that require safety and adaptability to unstructured environments. Specifically, programmable soft materials that can reconfigure their shapes, properties, or functionalities

In this context, other approaches have integrated stimuli-responsive smart materials such as shape memory polymers (SMPs),^[25] liquid crystal elastomers (LCEs),^[26] magnetorheological fluids,^[27] and phase-changing materials^[11,28] to provide metamaterials with more diversified in situ programmable functionalities. These reconfigurable mechanical metamaterials can change their physical properties, such as shapes,^[29] curvatures,^[11] and stiffness^[21] under external stimuli. However, still they usually have limited mechanical capability to perform under different situations that require strategic and timely adjustments in functionality, due to the inherently limited stable physical states (or memory) of the smart materials. Therefore, in practice, achieving a wide variety of (or imminently required) physical properties of a soft programmable material, both qualitatively and quantitatively, in real-time still presents a challenge.

Here we introduce an encodable digital mechanical metamaterial that provides in situ and gradational tunability in various mechanical qualities such as shape-shifting and -memory, stress–strain response, and Poisson's ratio under compressive load, all

J. K. Choe, J. Yi, H. Jang, H. Won, S. Lee, H. Lee, Y. Jang, H. Song, J. Kim
Department of Materials Science and Engineering
Ulsan National Institute of Science and Technology (UNIST)
Ulsan 44919, Republic of Korea
E-mail: jiyunkim@unist.ac.kr

J. Kim
Center for Multidimensional Programmable Matter
Ulsan National Institute of Science and Technology
Ulsan 44919, South Korea

 The ORCID identification number(s) for the author(s) of this article can be found under <https://doi.org/10.1002/adma.202304302>

DOI: 10.1002/adma.202304302

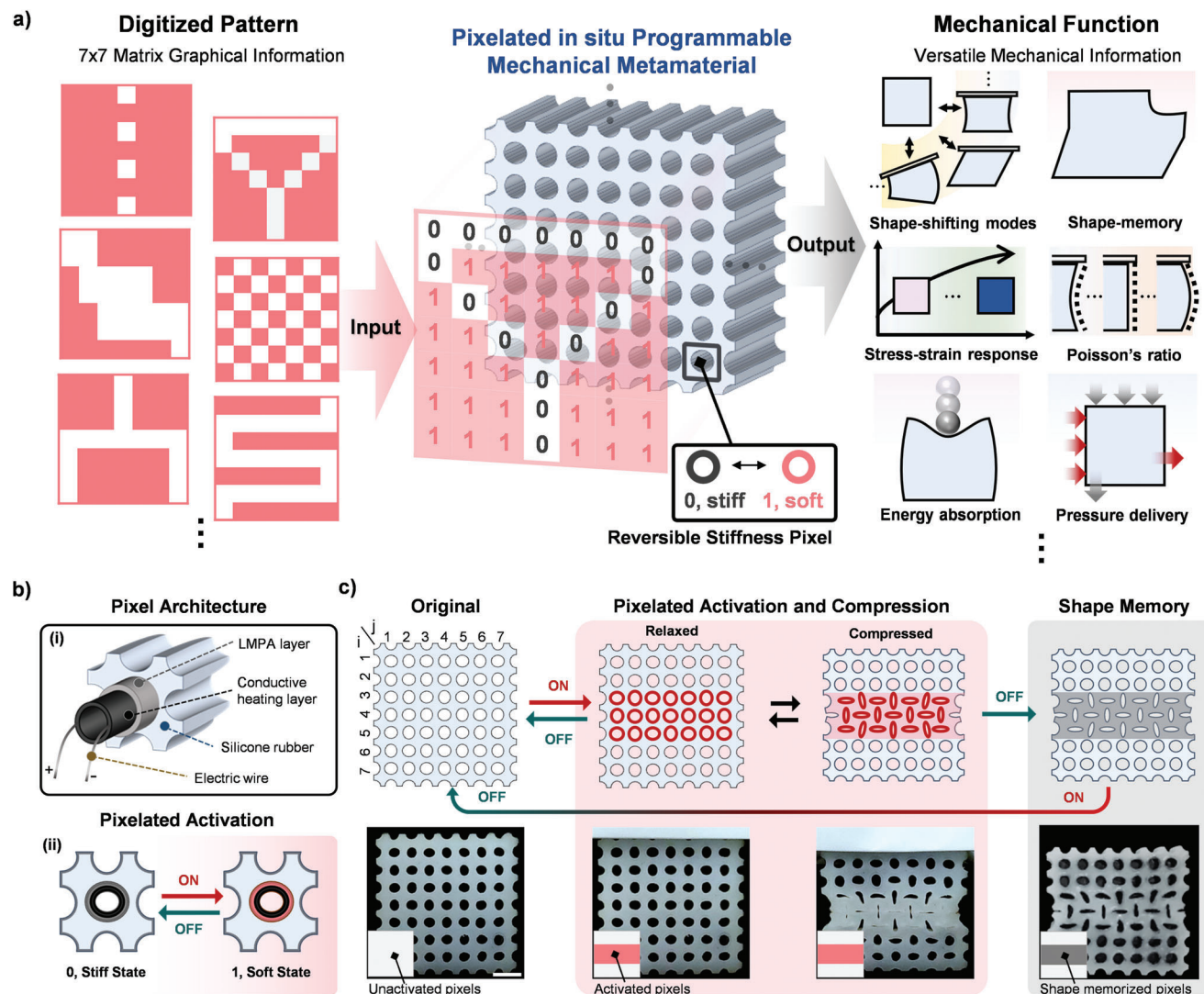


Figure 1. Concept and mechanism of PPMM in situ programming of mechanical behaviors. a) The design concept of using digital patterns of binary numbers “0” and “1” to project versatile mechanical information. The binary information of a digital pixel is translated to discrete stiffness states of the corresponding mechanical pixel. A schematic gallery of several mechanical capabilities is shown derived from various digitalized pattern instructions. b, i) Mechanical pixel architecture and ii) reversible stiffness mechanism using phase transition of the LMPA layer. c) Operating processes for developing reprogrammable mechanical functionalities and exemplary shape reconfiguration and shape memory effect of the PPMM.

in a single metamaterial system. Inspired by binary language systems where simple coding of discrete binary digits with assigned coding sequences enables effective and comprehensible representations of a variety of information, we harness stiffness tunable pixels that can be in situ encoded as “0” (stiff) and “1” (soft), to translate digitized stiffness pattern information of $(i \times j)$ pixels into $(2^{i \times j})$ possible mechanical information (Figure 1a). We note that these pixelated or combinatorial approaches have been tried before,^[30–38] but in situ programmability and mechanical capability were not fully explored or achieved. A detailed comparison of our mechanical metamaterial with state-of-the-art is shown in Table S1 in the Supporting Information. To further achieve such a wide range of programmability, we developed the digital mechanical metamaterial composite that synergistically combines elastic instability behaviors of elastomeric

endoskeleton with a periodic array of elliptical voids and the phase change of embedded low-melting-point alloy (LMPA) pixels. These LMPA pixels, with their two extremely contrasting stiffness states (liquid or solid),^[28] empower the distinctive effects of each digital state of the pixels that can be critical for achieving versatility when using stiffness patterning. Finally, reversibility is achieved by integrating heaters into each pixel to actively control the phase transition of the LMPA.

While the endoskeleton of our metamaterial is a simple and widely known structure for its auxetic (or negative Poisson’s ratio) behavior,^[16] we show that encoding different stiffness patterns unravels diverse and gradually tunable mechanical functions that can be achieved in a programmable and coherent manner. For example, the digitized stiffness patterns enable rich shape reconfigurability of the material under load, releasing numerous

shape-shifting modes such as contraction, shear, and flexure, all of which degree of shape reconfiguration can be tuned in a gradual manner. The morphed shape can be further permanently memorized globally or locally without requiring external energy inputs for potential load-bearing applications. In addition, we show that local stiffness tuning can be leveraged for the global mechanical characteristics, enabling gradational control of the stress–strain curve and Poisson’s ratio of the material between two extreme states. Finally, we demonstrate this material as a tunable and reusable energy absorption material that can provide the least transmitted stress for different impact scenarios and pressure delivery material that can reprogram the pressure flow path and sequence within the material for the delivery of pressure to specific locations and time under external loads. We expect that this digital mechanical metamaterial will pave the way for the creation of soft robots and machines that can dynamically adapt to their surroundings and operate effectively in unstructured environments.

2. Results and Discussion

2.1. Platform Development

The concept prototype, which we refer to as a “pixelated in situ programmable mechanical metamaterial (PPMM),” consists of a 7×7 periodic composite array with alternating elliptical voids, a common structure known to exhibit buckling-induced re-entrant behavior under compressive load. Each unit structure is comprised of three layers: an embedded LMPA layer, a conductive heating layer, and a silicone rubber layer, as shown in Figure 1bi. The LMPA layer is a eutectic alloy of bismuth, indium, and tin that can demonstrate a dramatic shift in stiffness from a solid with a high elastic modulus (>3 GPa) to a flowable liquid at the melting temperature of 61 °C. The conductive heating layer is a mixed composite of an elastomer and carbon black (9 wt%), allowing conduction (see Figure S2, Supporting Information) while retaining elastomeric mechanical properties (see Figure S3, Supporting Information). The LMPA layer is discretely embedded inside each pixelated void of the silicone rubber endoskeleton and actively controlled by the conductive heating layer with flowing current (Joule heating) to control the digital states “0” and “1” of each pixel, as shown in Figure 1bii.

By simply uploading a digital pattern of activation instruction, the PPMM can read and selectively control the stiffness of each pixel (see Figure S3, Supporting Information) to generate specific mechanical responses. For example, in shape-shifting scenarios, the inactivated solid-state LMPA layers prevent reorganization of the porous network under compression, whereas the activated liquid-state LMPA layers allow the voids to collapse and produce local reconfigurations. Furthermore, a shape memory behavior can be derived by returning the activated pixels to the solid state while retaining the compressive load. In Figure 1c, mechanical pixels at horizontal three middle rows of the PPMM ($i = 3-5$, $j = 1-7$, where i and j represent the column and row numbers, respectively) were activated and compressed. As a result, the PPMM was reconfigured into an “hourglass” shape, with the buckling-induced auxetic configurations at the activated regions while other inactivated regions stayed relatively undeformed. Upon deactivating pixels while maintaining compressive

load, the PPMM underwent phase transition back to a solid state within a few minutes (see Figure S2, Supporting Information) and then memorized the deformed shape without consuming external energy. Then, reheating the deactivated pixels returned PPMM to the original shape from the shape-memorized state. Since these shape-shifting and shape-memory responses (as well as other mechanical responses that can be displayed) are reversible, the PPMM can be reprogrammed to create a different shape or serve a different mechanical function without requiring new mechanical infrastructure by simply returning the PPMM to its original state and then uploading a new control pattern instruction.

2.2. Shape Reconfiguration and Memorization

By rationally encoding the digital pattern of the mechanical pixels, numerous sets of shape-shifting modes of the PPMM can be expressed. In Figure 2a, we show several possible modes under a compressive load: stationary, contraction, shear, and flexure modes (see Movie S1, Supporting Information). Numerical investigations were performed using finite element analysis (FEA) to simulate the shape-shifting behavior of individual digital patterns (see the Experimental Section “Finite Element Simulations”). The simulation results were in good agreement with the experimental results.

The reconfiguration of the mechanical pixels within the PPMM is dominantly determined by the activated pixels and their adjacent digital state pixel patterns. Specifically, the homogeneously inactivated pattern substantially inhibited the reconfiguration of the entire voids (Figure 2ai), whereas the homogeneously activated pattern with no adjacent stiff pixels promoted contraction under compressive load driven by buckling-induced orthogonally symmetrical re-entrant reconfigurations (Figure 2aaii). The two characteristic contractability created by these homogeneous patterns can be further blended through a mixed design of their patterns, distributed block-wisely from top to bottom. As shown in Figure 2b and Figure S5a in the Supporting Information, the contractability is tuned stepwise depending on the ratio of the inactivated and activated rows of pixels.

Furthermore, the reconfiguration shape of the activated pixels can be systematically programmed by tuning the adjacent boundary conditions. For example, the orthogonally symmetrical reconfigurations in Figure 2aaii can be broken with a diagonally activated pattern, which instead produce synchronously inclined re-entrant reconfigurations and subsequent macroscopic shear (Figure 2aiii). This lateral sliding motion under the compressive load can be quantitatively (and perhaps directionally) adjusted by the slope of the diagonally activated pattern, allowing stepwise tunability in shear angle Φ , as shown in Figure 2c and Figure S5b in the Supporting Information.

Lastly, the digital patterns can be encoded from a spatial perspective to achieve local variations in response. For example, a stepwisely activated pattern can derive a gradient in contractability along the columns ($j = 1-7$) of the PPMM, producing the flexure mode (Figure 2aiv). This gradient in contractability can be further adjusted, as shown in Figure 2d and Figure S5c in the Supporting Information, to achieve a quantitative spectrum in flexure angle θ .

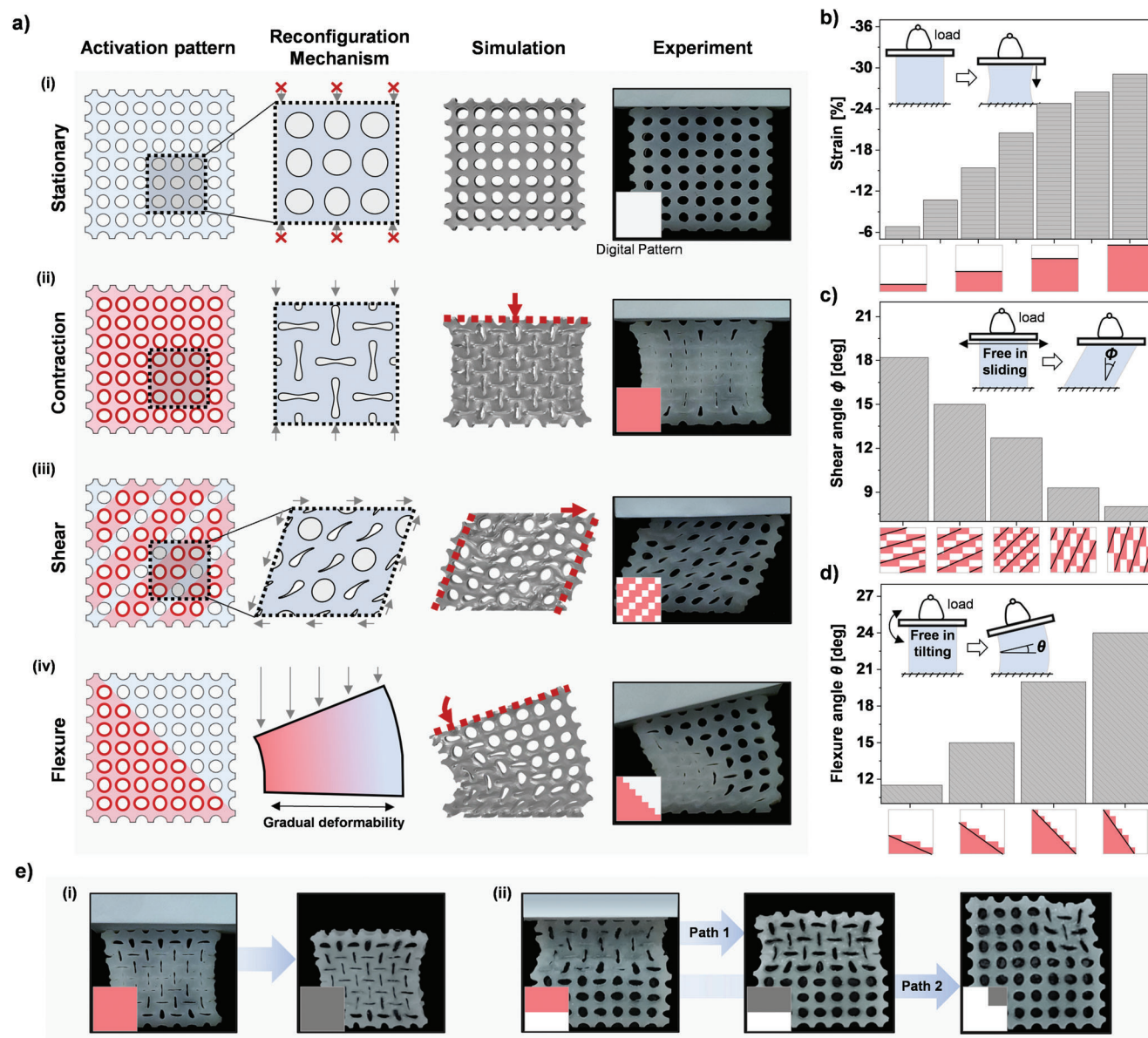


Figure 2. Shape-shifting and shape-memory capabilities. a) Schematic illustration of various producible shape-shifting modes with simulation and experimental results. b–d) Quantitative programming of various shape-shifting parameters: b) contractability, c) shear angle Φ , and d) flexure angle θ . Digital patterns are explored and developed while preserving each reconfiguration mechanism to achieve stepwise tunability. Compressive load = 1 kg. e) Schematic of digital patterns and experimental images demonstrating shape memory capabilities of the PPMM: i) homogeneous shape memory and ii) partial shape memory (path 1) and additional selective shape memory (path 2).

In addition to the spatial coding of the mechanical pixels, a time-dependent coding with rationally sequenced digital patterns and loads can excavate versatile shape-memory functionalities of the PPMM (Figure 2e). Along with the monotonous shape memory of the entire structure (Figure 2ei), the pixelated control enables localized activation of the PPMM as shown in Figure 2eii, which can be homogeneously memorized (path 1) or selectively memorized (path 2). We note that by combining this memorization capability with shape tunability, heterogeneous shape memorization within a single structure could possibly be achieved

with spatially distributed shape retaining of differently shape-shifted pixels.

2.3. Mechanical Property Tuning and Decoupled Responses

Another quality that can be gradually tuned with digital pattern coding is mechanical properties. **Figure 3a** shows the PPMM with gradually activated rows of pixels under the same compressive pressure (10 kPa). Here, along with the contractability shown

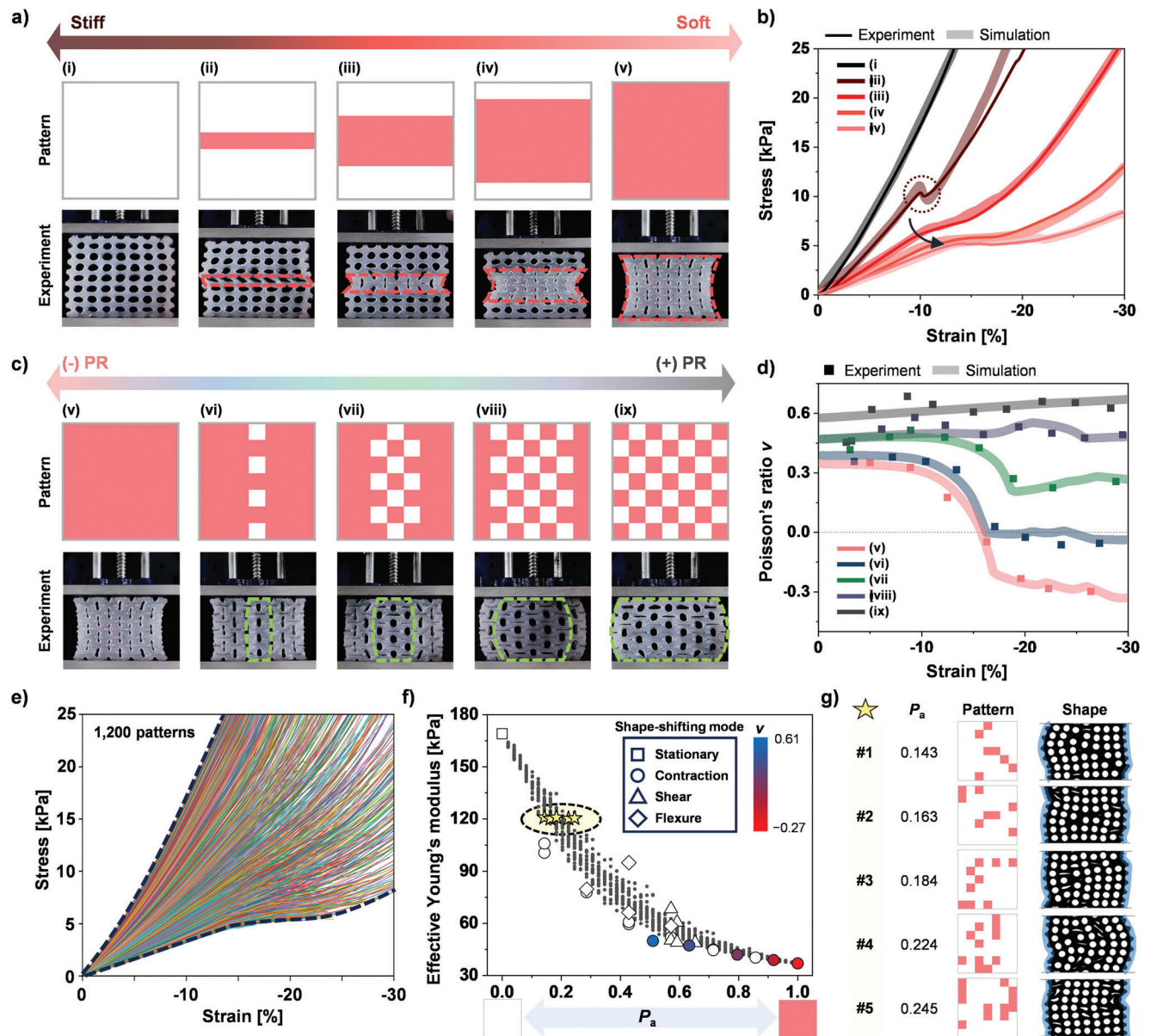


Figure 3. Mechanical property programming and decoupled responses. a) Schematic and experimental images of PPMM with progressively activated rows of pixels from (i) to (v). Images are taken at strain $\varepsilon = -5\%$, -10% , -15% , -20% , and -25% , respectively. Dotted red lines correspond to mechanical pixels with the soft response. b) Stress–strain curve for various patterns in (a). The dashed circle indicates the abrupt local minimum and the arrow indicates the gradual emergence of the nonlinear plateau. c) Schematic and experimental images of PPMM with increasing columns of alternative checkboard pattern from (v) to (ix). All images are taken at strain $\varepsilon = -30\%$. Dotted green lines correspond to local augmented positive Poisson's ratio behaviors. d) Poisson's ratio as a function of strain for various patterns in (c). e) Stress–strain response of 1200 simulations, showing fine-tunability of the PPMM. f) Effective Young's modulus Y as a function of activated pixel density p_a . Selected patterns with rare-event shape deformation modes and tunable Poisson's ratios ν are highlighted. g) Five patterns selected in (f), indicated by a dotted ellipse, that show similar Effective Young's modulus Y but distinct deformation shapes. Shape images are captured at -24.3% strain.

in Figure 2b, rigid inactivated pixels and soft activated pixels (indicated by the red dotted line) can be blended to create gradual tunability in global mechanical elasticity. Figure 3b shows the stress–strain (σ – ε) curves of the above patterns from uniaxial compression tests. Effective Young's modulus Y was evaluated from the initial slope of the stress–strain curves. The PPMM with a homogeneously inactivated pattern showed a rigid response ($Y_{(i)} = 171.2$ kPa). In comparison, the liquid-state homogeneously

activated pattern showed a soft response ($Y_{(v)} = 38.9$ kPa), which is 4.4 times softer than the homogeneously inactivated state. Within this obtained range of tunability, the intermediate partially activated patterns showed mechanical properties between the two extreme homogeneous patterns depending on the compositional ratio of the soft activated pixels.

Furthermore, the shape of the stress–strain curve was programmed depending on the dominant reconfiguration

mechanisms of the mechanical pixels. In detail, the homogeneously inactivated pattern (Figure 3ai) showed a relatively linear stress–strain response, with the silicone layer’s compression as the dominant mechanism that resists the compressive load. For the PPMM with activated pixels at $i = 4$ (Figure 3aii), the boundary conditions of the activated pixels produced a bistable snap-through behavior that led to an abrupt local minimum (indicated by the dotted circle in Figure 3b) at a critical strain. Lastly, for the activation patterns that create symmetrical re-entrant reconfigurations of the activated pixels (Figure 3aiii–v), a nonlinear plateau (where the structure contracted with minimal additional strain energy) emerged driven by instability-induced buckling. The plateau region evolved gradually with greater flattening behavior as the number of activated rows increased (indicated by the dashed arrow in Figure 3b).

As another mechanical property of the PPMM, we explored the effect of pixelated activation on the Poisson’s ratio ν . To achieve gradational tunability in ν , a coherent approach was taken: first, deriving two elemental patterns that generate opposing characteristics in Poisson’s ratio (negative and positive; see Movie S2, Supporting Information), then blending the patterns for the intermediate quantities. Figure 3c shows the PPMM with gradually activated columns of pixels with an alternative checkboard pattern under the same compressive strain ($\epsilon = -30\%$). Here, we modified the mutually orthogonal re-entrant mechanism that creates a negative Poisson’s ratio (Figure 3cv) with the checkboard pattern that allows the pixels to buckle only in the horizontal direction, leading to an augmented positive Poisson’s ratio behavior (Figure 3cix). We note that this positive Poisson’s ratio was larger than that of the homogeneously inactivated pattern shown in Figure 3ai (see Figure S7, Supporting Information), demonstrating that our approach to material programming may facilitate the realization of unique properties beyond the commonly known auxetic properties of the design structure, within a single metamaterial system.

Blending these patterns column-wisely retained each distinct mechanism, allowing for local variations in Poisson’s ratio response (indicated by the green dotted lines for the positive Poisson’s ratio responses), which may be summed or canceled to produce the overall Poisson’s ratio response. The evolution of the global Poisson’s ratio ν is plotted as a function of strain in Figure 3d. The Poisson’s ratio was determined by calculating and averaging local Poisson’s ratios within the PPMM (see the Experimental Section “Mechanical Characterization” and Figure S8, Supporting Information). The initial Poisson’s ratio of each activation pattern was narrowly distributed ($\nu = 0.4 \pm 0.06$) at a relatively low compressive strain. However, when the buckling transformations were completed ($\epsilon \approx -20\%$), their Poisson’s ratios saturated at different values distributed over a wide range created by the two extreme patterns ((v): $\nu = -0.273$ and (ix): $\nu = 0.614$), including a near zero value ((vi): $\nu = -0.08$).

Finally, to gain a deeper understanding of the correlation between digital patterns and their associated properties, we conducted an extensive series of 1200 simulations, each featuring different patterns. The collection of patterns had a uniformly distributed activated pixel density p_a (calculated by the number of the activated pixels divided by the total number of pixels) and within each pattern, the activated pixels were distributed randomly. Also, we included specific patterns that were previously

shown, including those in Figure 3a,c, and the results were in good agreement with the experimental results (Figure 3b,d, respectively). The simulation results contained stress–strain curve and deformed shape data for each pattern. As a result, the PPMM showed a remarkable fine-tunability (Figure 3e), with each digital pattern having a distinctive set of stress–strain and shape-shifting responses. Also, the effective Young’s modulus Y and the activated pixel density p_a were inversely correlated (Figure 3f). Regarding shape deformation, the categories that we adopted (e.g., shear and flexure mode) were rare events that we discovered by rationally encoding the digital patterns out of the extensive 2^{49} possible patterns. Similarly, patterns with calculable Poisson’s ratios were also rare events because the deformation necessitates no change in the transversal strain under periodic boundary assumptions to apply the notion of Poisson’s ratio. In practice, in our dataset of 1200 observations, most patterns showed complex and combinatorial shape-tunable continuous curves on the left and right sides of the PPMM (Figure 3g). Harnessing this substantial tunability, we uncovered the ability to customize the shape-shifting behavior of the PPMM while maintaining a nearly consistent effective Young’s modulus Y (indicated by dotted Ellipse in Figure 3f,g). This versatility holds promise for the adaptation of the PPMM to suit specific application requirements.

2.4. PPMM as an Adaptive Energy Absorption Material

We demonstrate the PPMM as a tunable and reusable energy absorption material for an extensive range of possible impact scenarios. While most existing energy absorption materials have fixed mechanical properties, attenuating specific impact through irreversible crushing or plastic deformation, the PPMM features reprogrammability with facile tuning capability and recoverability driven by the phase-transition mechanism.

Here, different fractions of inactivated and activated pixels were evenly dispersed within the digital pattern to achieve different mechanical elasticity while avoiding severe local stress concentration (Figure 4ai). An energy absorption material that is excessively soft or rigid for a given impact energy results in high transmitted stress (see Figure S9, Supporting Information) that might cause damage or injury. Specifically, at low impact energies (Figure S9bi, Supporting Information), rigid materials absorb energy elastically but transmit higher stress. In contrast, soft materials absorb the same energy with more deformations, leading to reduced transmitted stress. However, at high impact energies (Figure S9biii, Supporting Information), soft materials may deform excessively and enter the densification region, which significantly increases the transmitted stress. Thus, rigid materials are more advantageous in such cases. In this context, the customizable stress–strain response (Figure 4aii) of the PPMM could offer optimal performance with the least possible transmitted stress in an arbitrary impact scenario. For example, the optimal digital pattern for a scenario with relatively high impact energy can be achieved by adequately reducing the activated pixel ratio (to increase the effective stiffness). To validate this, the absorbed energy E as a function of peak transmitted stress was plotted for each activation pattern (Figure 4aiii). E was evaluated as the area under the experimentally obtained stress–strain curve in Figure 4c. Finally, a design map (shaded regions in Figure 4aiii)

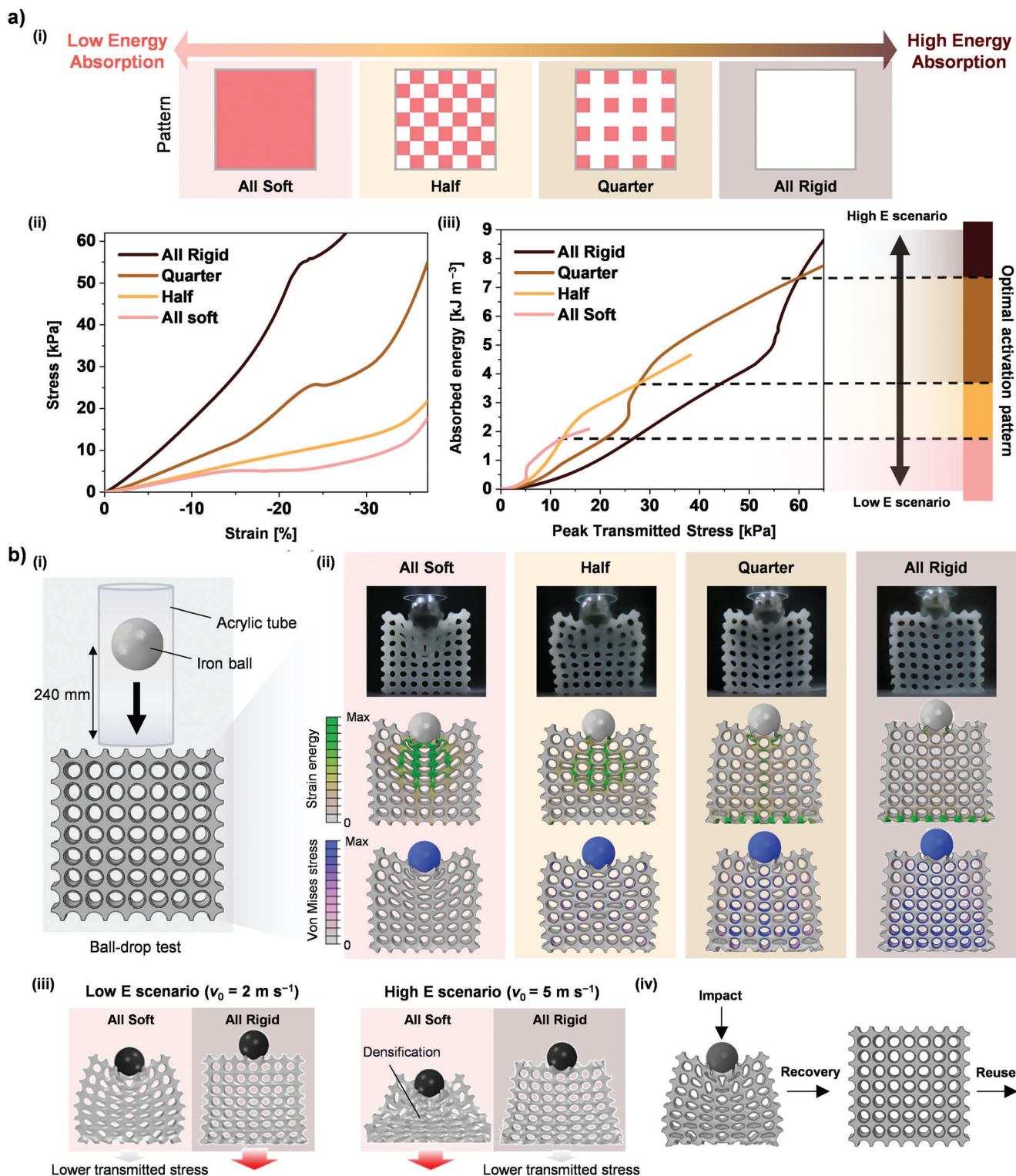


Figure 4. PPMM as an adaptive and reusable energy absorption material. a.,i) Digital patterns with various proportions (100%, 50%, 25%, and 0%) of evenly distributed activated pixels, ii) corresponding stress–strain curve obtained from experiment, and iii) energy diagram (left) and schematic (right) guiding optimal activation pattern that minimizes transmitted stress for different impact energy scenarios. b.,i) Schematic of a ball-drop impact scenario and ii) experiment and simulation results of various digital patterns after a 14 ms contact duration. iii) Simulation results at low impact energy and high impact energy scenarios. iv) Schematic of PPMM recovering after an impact to be reused for a different task.

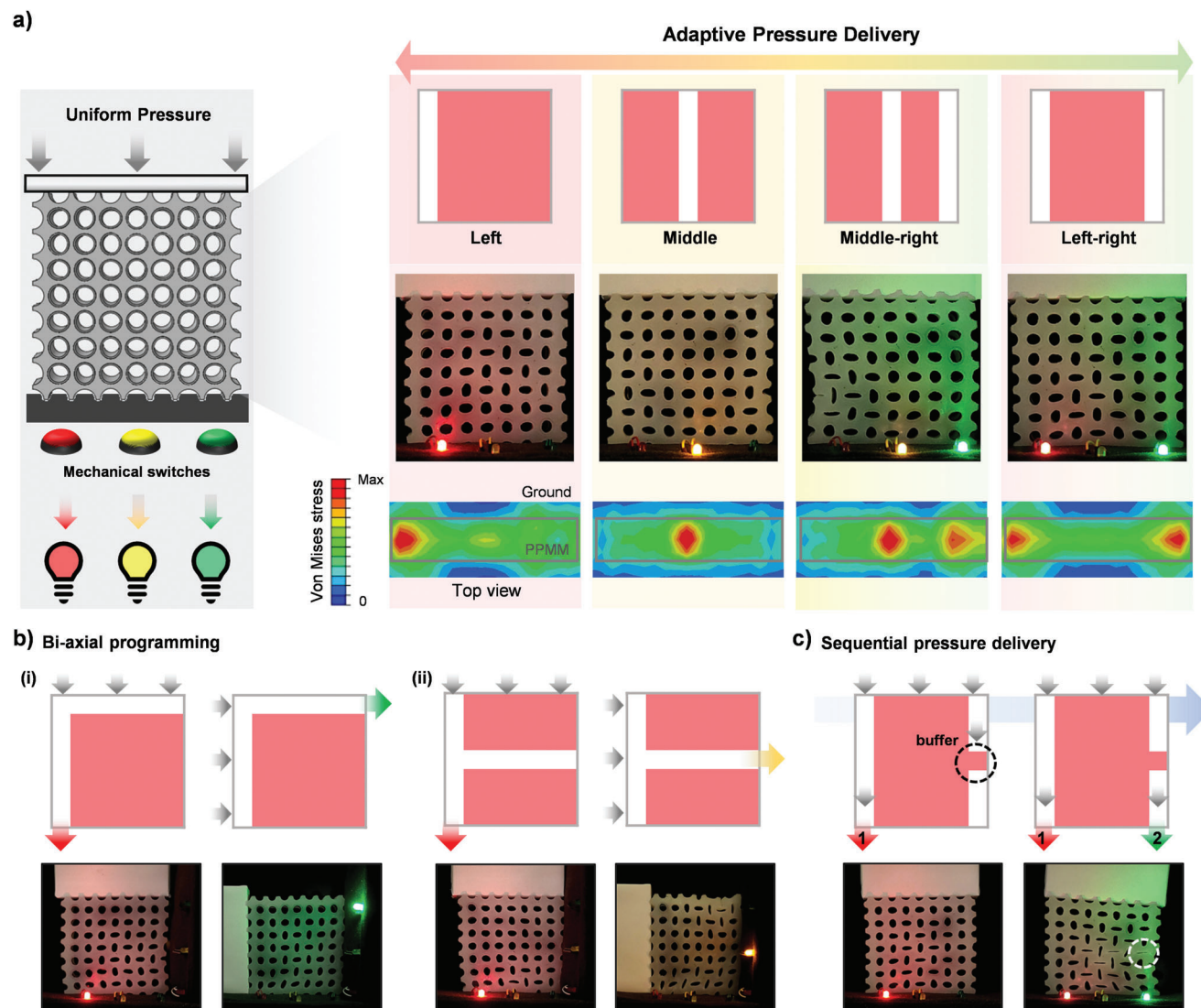


Figure 5. PPMM as an adaptable pressure delivery material. a) Schematic, experiment, and simulation results of various digital patterns controlling the path of the stress flow within the PPMM. Gray boxes in simulation results represent outlines of the PPMM. b) Biaxial stress flow path programming with independent horizontal and vertical tunability. The horizontal path is tuned i) from operating the green LED ii) to the yellow LED, while maintaining the vertical path. c) Pressure delivery sequence programming. The operation of the green LED is delayed by incorporating a buffer pixel (indicated by the dotted circle).

that guides the optimal activation pattern (with the minimum peak transmitted stress) was plotted over a range of E , demonstrating the capability of the PPMM to fit in different conditions.

In Figure 4bi, the feasibility of the PPMM as an adaptive energy absorption material was verified through a simple case study in which an iron ball (0.55 kg), guided by an acrylic tube, was dropped from a height of 240 mm onto the PPMM (Figure 4bi). As shown in Figure 4bii, the PPMM with the higher composition of activated pixels responded with higher deformation during impact. Simulations were performed to further assess the distribution of internal strain energy and internal stress within the PPMM during impact. For simplification, the iron ball was dropped at the initial speed of $v_0 = 2 \text{ m s}^{-1}$ from a height of 40 mm onto the PPMM in simulations, which closely approximate the impact energy levels that occurred in the experiments.

As a result, the PPMM with the higher composition of activated pixels responded with higher deformation with more distributed strain energy within the silicone layer (shown in green contour). However, within the same structure, the PPMM with the lower composition of activated pixels responded with higher internal stress distributed within the solid LMPA layers (shown in blue contour). The deformation shapes in simulations were in reasonable agreement with the experimental results. These findings suggest that deformation of the structure within the elastic region can effectively absorb energy and avoid creation of internal stress that can elevate the transmitted stress (Figure 4biii, left). However, in higher impact energy scenarios (e.g., ball drop speed of 5 m s^{-1}), highly deformable patterns could be less advantageous as excessive deformation can lead to the densification of the structure (Figure 4biii, right and Movie S3, Supporting Information).

These results align with the observations in Figure 4a_{iii}, indicating that the effectiveness of an activation pattern depends on the energy level of the impact scenario. Consequently, the PPMM can adaptively reduce transmitted stress in various impact scenarios through the adjustment of the activation pattern. We note that the deformed PPMM after the impact (even with local LMPA fractures, in principle) can be recovered through liquefaction and further reused (Figure 4b_{iv}), which can be advantageous in terms of sustainability and resource efficiency.

2.5. PPMM as an Adaptive Pressure Delivery Material

As another possible application, we exploit the PPMM as an adaptive pressure delivery material that can control the path of stress flows through their mechanical pixels. In detail, when one side of the PPMM is pressed, the pressure can be selectively transferred to specific locations on the other side depending on the encoding of digital patterns. In Figure 5a, we visualize the concept of the pressure delivery material using mechanical switches connected to light-emitting diodes (LEDs) of different colors (see Figure S10, Supporting Information). When the pressure was applied to the top of the PPMM, the pressure was exclusively transferred to the bottom near the rigid mechanical pixels (where the inactivated column pattern is located), turning on the matching light-emitting diode (see Movie S4, Supporting Information). The stress distribution of the base ground below the PPMM (without mechanical switches) was simulated for each activation pattern with uniformly applied pressure (shown by the contour map; see Figure S11, Supporting Information). The simulation results corresponded well with the experimental result.

In addition, this functionality can be extended to a biaxial basis, in which the pressure delivery path is programmed independently for each axis (horizontal and vertical). As shown in Figure 5b, the horizontal pressure flow path located at the top (Figure 5b_i) was changed to the intermediate position (Figure 5b_{ii}) while maintaining the vertical pressure path.

Lastly, we demonstrate that the pressure delivery can also be chronologically controlled by the activation pattern. As shown in Figure 5c, the inclusion of a buffer pixel (indicated by the dotted circle) delayed the transmission of the pressure driven by the deformation of the buffer pixel, resulting in sequential pressure delivery and subsequent operation of the LEDs.

3. Conclusion

We introduced a metamaterial composite system that allows for gradational and reversible adjustments in various mechanical information by translating encoded digital pattern information into discrete stiffness states of the mechanical pixels. Using this approach, the mechanical response of the material can be in situ reprogrammed with a broad design space of $2^{i \times j}$ possible patterns. In addition to this extensive range of possibilities, we synergistically combined i) an elastomeric endoskeleton with elastic instabilities, ii) LMPA that can reversibly transition between two vastly disparate stiffness states, and iii) a soft heater to demonstrate the PPMM as a digital mechanical material platform that unravels numerous mechanical capabilities, controlled simply by

uploading abstracted digital geographic patterns with spatial and sequential variations. FEA simulations were conducted to aid the prediction of mechanical behaviors created by digital stiffness patterns.

Specifically, while some digital patterns could lead to geometric frustration (which is conventionally avoided as they hinder coherent operation), we exploited aperiodicity in mechanical pixels with different stiffness boundary conditions to achieve functionalities such as shear and flexure shape-shifting modes. The encoding of digital patterns as a function of time also excavated uncommon functionalities, such as partial shape memorization, which could be used for localized memorization of different shapes to create various load-bearing shapes. We found several coherent and comprehensible relationships between digital patterns and output mechanical behaviors. For example, two patterns that generate distinct quantities in effective Young's modulus or Poisson's ratio were partially blended to create a new pattern that produces an intermediate quantity. Finally, several practical scenarios were demonstrated in which the PPMM adapts as an energy absorption or pressure delivery material and dynamically performs tasks according to more specific assignments.

Overall, our combinatorial metamaterial that achieves numerous in situ programmable mechanical capabilities whose information is abstracted in digitized stiffness pattern information represents a stepping stone for a universal, adaptable, and sustainable mechanical metamaterial. We note that while the frame structure of the PPMM that allows modulation of re-entrant buckling mechanisms of each elliptical void was recognized for its broad-range tunability particularly in Poisson's ratios, we note that the frame structure, pixel locations, and pixel shapes could be highly varied (Figure S12, Supporting Information) to potentially abstract different specialized mechanical information within the digital patterns. Also, along with our FEA simulations, we expect a faster prediction and full exploration of mechanical responses in the future through using artificial intelligence such as a convolutional neural network since the mechanical information can be represented by pattern images. Also, through combining the use of optimization algorithms, we envision the potential to work toward the inverse design of stiffness patterns for diverse dynamic and adaptation-critical situations. We anticipate that this work will inspire the development of cognitive mechanical metamaterials that can autonomously percept, process, and learn,^[39] which may be realized in the future through technological advancements with embedding pixelated devices such as sensors^[40–42] and processors^[3,43] with artificial intelligence algorithms.^[44]

4. Experimental Section

LMPA Layer Preparation: Conventional molding techniques were used to prepare the LMPA layer. For a simple demolding process, first, a pre-mold is printed for the LMPA layer with polyvinyl alcohol (PVA) using a 3D printer (Ultimaker 2). Then, a soft silicone rubber (Ecoflex 00-30; Smooth-On) was cast into the pre-mold and cured for 1 h in an oven at 80 °C. The silicone structure was demolded to be used as the LMPA layer mold.

Next, liquidized LMPA (Bolton, Field's metal) was injected into the ring-shaped voids of the silicone mold with a syringe. The mold was placed on a hotplate during injection to prevent the solidification of the LMPA.

Finally, the mold was placed at room temperature to solidify the LMPA layer for 10 min and then the silicone mold was removed. The LMPA layer is a hollow elliptic cylinder with a major axis of 1.04 mm, a minor axis of 0.96 mm, a thickness of 0.4 mm, and a height of 15 mm.

Conductive Heating Layer Preparation: Ecoflex 00-30 (Smooth-On) and carbon black (Super P, Alfa Aesar) were mixed (weight ratio = 100:9) at room temperature to make the conductive sludge. The sludge was placed on a flat aluminum foil and then spread into a 0.25 mm thick layer using a micrometer-adjustable film applicator. Two lead wires were placed 13 mm apart in the middle of the sludge, then more sludge was poured onto the fixed wires and spread into a 0.6 mm thick layer. Finally, the sludge layer was placed on a hotplate at 80 °C for 1 h and cut into a rectangular shape with a size of 34 mm × 30 mm.

PPMM Fabrication: First, a structural mold with the size of 104 mm × 104 mm × 60 mm (length × width × height) and a total of 49 elliptic pillars with the size of 0.88 mm × 0.8 mm × 60 mm (major axis × minor axis × height) were 3D printed (Ultimaker 2) with PVA. The structural mold has a 7 by 7 periodic array of craters at the bottom (depth of 20 mm) that can clinch the elliptic pillars.

Then, the prepared conductive heating layer was rolled into a cylindrical shape and attached to the inner surface of the LMPA layer using silicone adhesive (Sil-Poxy; Smooth-On), followed by the insertion of the printed elliptic pillar. This procedure was repeated to create 49 identical units, which were then clinched into the craters of the structural mold.

Hereafter, Ecoflex 00-30 was cast into the structural mold, degassed in a vacuum chamber for 25 min, and cured in an oven at 65 °C for 1 h. Finally, the printed pillars and the structural mold were removed to create the PPMM by submerging the whole structure underwater overnight. The overall fabrication process is illustrated in Figure S1 in the Supporting Information.

Electrical and Thermal Characterization: To find appropriate Joule-heating conditions for controlling the liquid–solid phase transition of the LMPA layer, the conductivity of the heating layer was characterized depending on the weight ratio between the soft silicone and the carbon black (Figure S2a, Supporting Information).

The electrical conductivity κ of the conductive heating layer was calculated as $\kappa = L A^{-1} R^{-1}$, where L is the length, A is the cross-sectional area, and R is the resistance. The resistance of the layer was measured with True root mean square (RMS) Multimeter (Fluke). The conductivity increased and subsequently saturated with increasing carbon black concentration. The optimal carbon black concentration was found as 9 wt%, which provided near-saturated conductivity while avoiding excessive viscosity that would encumber film production.

To activate the mechanical pixels, electricity was applied through corresponding lead wires using a DC power supply (Tektronix, PWS2326). To find the appropriate voltage condition, the structure was turned on and off repetitively for 400 s each and the temperature of the heating layer was trailed using a thermometer for various applied voltages (Figure S2b, Supporting Information). The voltage of 25 V was used, which raised the temperature above the melting point of the LMPA within a few minutes.

Shape Fixation and Recovery Rate Characterization: To investigate the ability of the LMPA to retain the deformed shape of PPMM and recover its original shape, the shape fixation rate R_f and shape recovery rate R_r were characterized (Figure S6, Supporting Information). The shape fixation rate R_f was defined as $R_f = \epsilon_u / \epsilon_f \times 100$ [%], where ϵ_u is the compressive strain of the sample after unloading and ϵ_f is the compressive strain at which the sample is fixed. Red dots were indicated above the $(i, j) = (1, 4)$ pixel and below the $(i, j) = (7, 4)$ pixel and tracked for calculation. To show the full capability of the PPMM, the samples were unloaded after 30 min of complete inactivation of the pixels for fixation. The shape recovery rate R_r was defined as $R_r = (\epsilon_f - \epsilon_r) / \epsilon_f \times 100$ [%], where ϵ_r is the compressive strain after recovery. ϵ_r was calculated after 10 min of complete activation of the pixels for recovery.

Mechanical Characterization: The stress–strain curves were obtained by conducting uniaxial compression tests on a universal electromechanical testing machine (AGX-100NX, SHIMADZU) at a loading rate of 1 mm s⁻¹. The stress σ was calculated by dividing the total applied force by

the initial cross-sectional area, and the strain ϵ was calculated by dividing the change in structure height by the original height.

For the analysis of the Poisson's ratio, the PPMM was marked with black dots, and their positions were video recorded and then analyzed by an image processing tool (image J). As shown in Figure S8 in the Supporting Information, 8 × 8 vertices around the 7 × 7 pixels were marked with black dots and tracked to calculate local values of engineering strain in both x and y directions using the following equations

$$\epsilon_x^{[i,j]} = \frac{(x^{(i,j+1)} - x^{(i,j)}) + (x^{(i+1,j+1)} - x^{(i+1,j)})}{2D_0} - 1 \quad (1)$$

$$\epsilon_y^{[i,j]} = \frac{(y^{(i,j)} - y^{(i+1,j)}) + (y^{(i,j+1)} - y^{(i+1,j+1)})}{2D_0} - 1 \quad (2)$$

where D_0 denotes the distance between vertices before the compressive load is applied.

Since the effect of the internal mechanisms can be reduced at the edges of the PPMM, the global Poisson's ratio for each sample was calculated from the median row of the PPMM (i.e., $i = 4$) to reduce the influence of the boundary conditions. Specifically, the global Poisson's ratio for each sample was determined by taking the ensemble average of seven local Poisson's ratios derived from the calculated local engineering strains as follows

$$\nu = \langle \nu^{[4,j]} \rangle = \left\langle -\frac{\epsilon_x^{[4,j]}}{\epsilon_y^{[4,j]}} \right\rangle \quad (3)$$

Finite Element Simulations: FEA was performed using the commercially available software Abaqus. To simulate various activation patterns of PPMM, the LMPA layer was modeled separately as solid phase and liquid phases, then selectively tie-constrained to each void in the endoskeleton silicone rubber layer.

In all simulations, the silicone rubber layer (Ecoflex 00-30) was constructed with hybrid solid elements of type C3D8RH, and the mechanical property was constituted using hyperelastic Yeoh model with the following parameter values:^[45] $N = 3$, $C_{10} = 5072 \text{ J m}^{-3}$, $C_{20} = -331 \text{ J m}^{-3}$, and $C_{30} = -15 \text{ J m}^{-3}$. The solid phase layer was constructed using an elastic model with the solid element of type C3D8R with the following parameter values: Young's modulus $Y = 9.25 \text{ GPa}$ and Poisson's ratio $\nu = 0.445$.

The activated liquid phase layer was modeled using the fluid-filled cavity model, where a hydraulic cavity pressure is applied to a thin membrane of Ecoflex 00-30. The liquid phase layer was constructed with the membrane element of type M3D4R with a hydraulic cavity inside the membrane (fluid bulk modulus $K = 28.5 \text{ GPa}$). For simplicity, the mechanical property of the conductive heating layer was assumed to be equal to that of the silicone rubber layer.

To predict the morphing behaviors of the PPMM, a rigid plate of 1 kg placed above the metamaterial was gradually descended by gravity to deform the PPMM. To predict the stress–strain response and Poisson's ratio, a rigid plate above the metamaterial was gradually descended. Reaction force and compression distance were recorded for stress and strain calculations, respectively and changes in local transversal distances were recorded for Poisson's ratio calculation. For energy absorption simulations, an iron ball of 0.55 kg with Young's modulus $Y = 213 \text{ GPa}$, and Poisson's ratio $\nu = 0.3$ was dropped on top of the PPMM with an initial distance of 40 mm and speed of 2 or 5 m s⁻¹. For pressure delivery simulations, a rigid plate placed on top compressed the PPMM, and the stress contour of the ground was captured at the compressive strain of 5%.

Supporting Information

Supporting Information is available from the Wiley Online Library or from the author.

Acknowledgements

This work was supported by National Research Foundation of Korea (NRF) grants funded by the Korean government (NRF-2020R1A2C2102842, NRF-2021R1A4A3033149, NRF-2019-Global Ph.D. Fellowship Program, and RS-2023-00302525), and the Fundamental Research Program of the Korea Institute of Material Science (PNK7630).

Conflict of Interest

The authors declare no conflict of interest.

Data Availability Statement

The data that support the findings of this study are available from the corresponding author upon reasonable request.

Keywords

adaptability, digital stiffness pattern, mechanical metamaterials, pixelation, programmability, shape shifting

Received: May 8, 2023
Revised: September 15, 2023
Published online:

- [1] H. Cui, D. Yao, R. Hensleigh, H. Lu, A. Calderon, Z. Xu, S. Davaria, Z. Wang, P. Mercier, P. Tarazaga, X. Zheng, *Science* **2022**, 376, 1287.
- [2] D. Yang, B. Mosadegh, A. Ainla, B. Lee, F. Khashai, Z. Suo, K. Bertoldi, G. M. Whitesides, *Adv. Mater.* **2015**, 27, 6323.
- [3] C. El Helou, P. R. Buskohl, C. E. Tabor, R. L. Harne, *Nat. Commun.* **2021**, 12, 1633.
- [4] S. Janbaz, F. S. L. Bobbert, M. J. Mirzaali, A. A. Zadpoor, *Mater. Horiz.* **2019**, 6, 1138.
- [5] H. Lee, Y. Jang, J. K. Choe, S. Lee, H. Song, J. P. Lee, N. Lone, J. Kim, *Sci. Rob.* **2020**, 5, eaay9024.
- [6] R. Baines, S. K. Patiballa, J. Booth, L. Ramirez, T. Sipple, A. Garcia, F. Fish, R. Kramer-Bottiglio, *Nature* **2022**, 610, 283.
- [7] D. S. Shah, J. P. Powers, L. G. Tilton, S. Kriegman, J. Bongard, R. Kramer-Bottiglio, *Nat. Mach. Intell.* **2020**, 3, 51.
- [8] D. Shah, B. Yang, S. Kriegman, M. Levin, J. Bongard, R. Kramer-Bottiglio, *Adv. Mater.* **2020**, 33, 2002882.
- [9] Q. Ze, S. Wu, J. Nishikawa, J. Dai, Y. Sun, S. Leanza, C. Zemelka, L. S. Novelino, G. H. Paulino, R. R. Zhao, *Sci. Adv.* **2022**, 8, eabm7834.
- [10] Q. Ze, S. Wu, J. Dai, S. Leanza, G. Ikeda, P. C. Yang, G. Iaccarino, R. R. Zhao, *Nat. Commun.* **2022**, 13, 3118.
- [11] D. Hwang, E. J. Barron III, A. T. Haque, M. D. Bartlett, *Sci. Rob.* **2022**, 7, eabg2171.
- [12] T. Frenzel, M. Kadic, M. Wegener, *Science* **2017**, 358, 1072.
- [13] L. Jin, A. E. Forte, B. Deng, A. Rafsanjani, K. Bertoldi, *Adv. Mater.* **2020**, 32, 2001863.
- [14] C. Coulais, A. Sabbadini, F. Vink, M. Van Hecke, *Nature* **2018**, 561, 512.
- [15] J. T. B. Overvelde, S. Shan, K. Bertoldi, *Adv. Mater.* **2012**, 24, 2337.
- [16] K. Bertoldi, P. M. Reis, S. Willshaw, T. Mullin, *Adv. Mater.* **2010**, 22, 361.
- [17] A. Farzaneh, N. Pawar, C. M. Portela, J. B. Hopkins, *Nat. Commun.* **2022**, 13, 1041.
- [18] B. Florijn, C. Coulais, M. van Hecke, *Phys. Rev. Lett.* **2014**, 113, 175503.
- [19] H. Zhang, X. Guo, J. Wu, D. Fang, Y. Zhang, *Sci. Adv.* **2018**, 4, eaar8535.
- [20] K. Bertoldi, M. C. Boyce, S. Deschanel, S. M. Prange, T. Mullin, *J. Mech. Phys. Solids* **2008**, 56, 2642.
- [21] J. U. Surjadi, Y. Zhou, T. Wang, Y. Yang, J.-j. Kai, Y. Lu, Z. Wang, *iScience* **2021**, 24, 102789.
- [22] J. Paulose, B. G.-G. Chen, V. Vitelli, *Nat. Phys.* **2015**, 11, 153.
- [23] B. Haghpanah, L. Salari-Sharif, P. Pourrajab, J. Hopkins, L. Valdevit, *Adv. Mater.* **2016**, 28, 7915.
- [24] H. Zhang, J. Wu, D. Fang, Y. Zhang, *Sci. Adv.* **2021**, 7, eabf1966.
- [25] C. Yang, M. Boorugu, A. Dopp, J. Ren, R. Martin, D. Han, W. Choi, H. Lee, *Mater. Horiz.* **2019**, 6, 1244.
- [26] A. Kotikian, R. L. Truby, J. W. Boley, T. J. White, J. A. Lewis, *Adv. Mater.* **2018**, 30, 1706164.
- [27] J. A. Jackson, M. C. Messner, N. A. Dudukovic, W. L. Smith, L. Bekker, B. Moran, A. M. Golobic, A. J. Pascall, E. B. Duoss, K. J. Loh, *Adv. Sci.* **2018**, 4, eaau6419.
- [28] Y. Hao, J. Gao, Y. Lv, J. Liu, *Adv. Funct. Mater.* **2022**, 32, 2201942.
- [29] Z. Zhao, C. Yuan, M. Lei, L. Yang, Q. Zhang, H. Chen, H. J. Qi, D. Fang, *Phys. Rev. Appl.* **2019**, 11, 044074.
- [30] H. Tao, F. Danzi, C. E. Silva, J. M. Gibert, *Extreme Mech. Lett.* **2022**, 55, 101832.
- [31] N. Kidambi, V. Agarwal, T. N. Tallman, K.-W. Wang, J.-H. Han, S. Shahab, G. Wang, *Active and Passive Smart Structures and Integrated Systems XIV*, Proc. SPIE, Bellingham, WA, Vol. 11376, **2020**, p. 419.
- [32] C. Coulais, E. Teomy, K. De Reus, Y. Shokef, M. Van Hecke, *Nature* **2016**, 535, 529.
- [33] T. Chen, M. Pauly, P. M. Reis, *Nature* **2021**, 589, 386.
- [34] A. Lazarus, P. M. Reis, *Adv. Eng. Mater.* **2015**, 17, 815.
- [35] F. Pan, Y. Li, Z. Li, J. Yang, B. Liu, Y. Chen, *Adv. Mater.* **2019**, 31, 1900548.
- [36] R. Poon, J. B. Hopkins, *Adv. Eng. Mater.* **2019**, 21, 1900802.
- [37] X. Xin, L. Liu, Y. Liu, J. Leng, *Adv. Funct. Mater.* **2021**, 32, 2107795.
- [38] G. Park, S. Kang, H. Lee, W. Choi, *Sci. Rep.* **2017**, 7, 41000.
- [39] H. Wang, M. Totaro, L. Beccai, *Adv. Sci.* **2018**, 5, 1800541.
- [40] J. Li, L. Fang, B. Sun, X. Li, S. H. Kang, *J. Electrochem. Soc.* **2020**, 167, 037561.
- [41] A. Mohammadi, Y. Tan, P. Choong, D. Oetomo, *Sci. Rep.* **2021**, 11, 24125.
- [42] C. Larson, B. Peele, S. Li, S. Robinson, M. Totaro, L. Beccai, B. Mazzolai, R. Shepherd, *Science* **2016**, 351, 1071.
- [43] T. Mei, Z. Meng, K. Zhao, C. Q. Chen, *Nat. Commun.* **2021**, 12, 7234.
- [44] H. Pahlavani, M. Amani, M. C. Saldívar, J. Zhou, M. J. Mirzaali, A. A. Zadpoor, *Commun. Mater.* **2022**, 3, 46.
- [45] Y. Elsayed, A. Vincenzi, C. Lekakou, T. Geng, C. M. Saaj, T. Ranzani, M. Cianchetti, A. Menciassi, *Soft Rob.* **2014**, 1, 255.